Received: 4 October 2022 | Accepted: 22 April 2023

DOI: 10.1002/jmv.28783

RESEARCH ARTICLE

JOURNAL OF MEDICAL VIROLOGY WILEY

Mapping and characterization of G-quadruplexes in monkeypox genomes

Higor Sette Pereira[1] | Darren L. Gemmill[1] | M. Quadir Siddiqui[1] | Gunjan Vasudeva[1] | Trushar R. Patel[1,2,3]

[1]Department of Chemistry and Biochemistry, Alberta RNA Research and Training Institute, University of Lethbridge, Lethbridge, Alberta, Canada

[2]Department of Microbiology, Immunology and Infectious Disease, Cumming School of Medicine, University of Calgary, Calgary, Alberta, Canada

[3]Li Ka Shing Institute of Virology, University of Alberta, Edmonton, Alberta, Canada

Correspondence
Trushar R. Patel
Email: trushar.patel@uleth.ca

Funding information
Natural Sciences and Engineering Research Council of Canada; Canada Research Chairs; Canada Foundation for Innovation

Abstract

Monkeypox virus (MPXV) is a double-stranded DNA virus from the family Poxviridae, which is endemic in West and Central Africa. Various human outbreaks occurred in the 1980s, resulting from a cessation of smallpox vaccination. Recently, MPXV cases have reemerged in non-endemic nations, and the 2022 outbreak has been declared a public health emergency. Treatment optionsare limited, and many countries lack the infrastructure to provide symptomatic treatments. The development of cost-effective antivirals could ease severe health outcomes. G-quadruplexes have been a target of interest in treating viral infections with different chemicals. In the present work, a genomic-scale mapping of different MPXV isolates highlighted two conserved putative quadruplex-forming sequences MPXV-exclusive in 590 isolates. Subsequently, we assessed the G-quadruplex formation using circular dichroism spectroscopy and solution small-angle X-ray scattering. Furthermore, biochemical assays indicated the ability of MPXV quadruplexes to be recognized by two specific G4-binding partners—Thioflavin T and DHX36. Additionally, our work also suggests that a quadruplex binding small-molecule with previously reported antiviral activity, TMPyP4, interacts with MPXV G-quadruplexes with nanomolar affinity in the presence and absence of DHX36. Finally, cell biology experiments suggests that TMPyP4 treatment substantially reduced gene expression of MPXV proteins. In summary, our work provides insights into the G-quadruplexes from the MPXV genome that can be further exploited to develop therapeutics.

KEYWORDS

genomic mapping, G-quadruplex, monkeypox, poxvirus, SAXS, TMPyP4

Higor Sette Pereira and Darren L. Gemmill contributed equally to this work.

1 | INTRODUCTION

Monkeypox virus (MPXV) belongs to the Poxviridae family and *Orthopoxvirus* genus, with the smallpox virus as a popular close-related human pathogen. Primarily transmitted through direct contact with infected humans or animal reservoirs, MPXV triggers a smallpox-like illness distinguished by premature enlargement of lymph nodes.[1] MPXV is a zoonotic vesicular-pustular malady first identified in humans in the Democratic Republic of Congo (DRC) in 1970.[2] Since then, the infection has been considered endemic in DRC, propagating the cases to central and western African nations.[3] Initially thought to be a Southern Hemisphere geographical disease, MPXV's first infected case in the midwestern United States was detected in 2003.[4] Although previously deemed a rare disease, MPXV has emerged as the most critical human *Orthopoxvirus* infection since the eradication of Smallpox in 1977,[1] and it is evolving into a global public health threat with increasing numbers of cases in more than 30 countries outside of Africa.[5] Currently, no approved treatment exists exclusively for MPXV and patients are guided to symptomatic medication.[6] Even though Smallpox vaccines can offer 85% protection against MPXV,[7] a continuous vaccination program was discouraged after determining the virus was incapable of maintaining itself in human populations.[8] An absence of surveillance measures and cessation of smallpox vaccination have weakened herd immunity and are likely contributing to the reemergence in non-endemic areas.[3,6] In its latest report, the Centers for Disease Control and Prevention confirmed a total of 86 231 monkeypox cases, with 98% of the cases identified in previously unaffected regions and locations.

Poxviridae family members carry a sizeable double-strand DNA genome in approximately 200 kbp that multiplies into the host cell and is organized within a Central conserved region flanked by left and right terminal regions that hold inverted terminal repeats (ITRs).[7] MPXV's large genome equivalently contains multiple open reading frames that encode the entire proteins responsible for viral replication, transcription, and virion assembly.[7] Clade I and Clade II, formerly known as Congo Basin and West Africa, respectively, compartmentalize MPXV genomes, and no meaningful reduction in size and content was observed by examining new draft genomes released from 2022 isolates.[6] However, structural features present in the MPXV genome are still poorly investigated, and most of the currently known details were deciphered in a comparison based on close-related Poxviridae representatives. Recent research shed light on an RNA quadruplex structure in the C9L gene that became unstable during the evolution course, which was believed to be a significant element in MPXV transmission.[9]

G-quadruplexes (G4s) are noncanonical DNA and RNA structures formed by guanine-rich sequences that fold into two or more consecutive quartets.[10] A G-quartet refers to four planar guanines separated in two equivalent tracts collectively interacting via Watson-Crick and Hoogsteen hydrogen bonds. G4 is formed by stacking two or more quartets and preferentially stabilized by monovalent cations (K^+ > Na^+ > Li^+) and disturbed by the presence of divalent cation, like Mg^{2+} and Ca^{2+}[11,12] DNA quadruplexes can fold into parallel, antiparallel, and hybrid topologies based on strand direction, likewise loop size and composition.[10] To facilitate computational screening of putative quadruplexes, a theoretical consensus sequence was established as follows G_{3+}-N_{1-7}-G_{3+}-N_{1-7}-G_{3+}-N_{1-7}-G_{3+}-N_{1-7}, where G is the guanosine tracts, and N is the nucleotide content inside the loop.[13] However, quite a few DNA and RNA quadruplexes were discovered and characterized in literature uncompliant within this consensus sequence.[14,15]

These noncanonical G4 structures have been identified in all domains of life, modulating critical human processes, such as replication, transcription, mRNA splicing, translation, and epigenetic regulation of the genome, as previously reviewed.[16,17] G4s have also been discovered across microbial genomes that play an essential role in facilitating immune evasion, radioresistance, virion secretion, and nitrate metabolism.[18] Targeting G4s is a promising strategy to control microbial infection by inhibiting critical pathways. By specifically targeting RNA G4, researchers identified a reduced level of Ebola virus L gene expression in a mini-genome system that impacts decreasing viral replication.[19] Moreover, in Herpes Simplex Virus-1 infected cells, DNA G4s were shown to participate in antiviral cellular defense pathways, and once those structures are stabilized, viral infection is diminished to controlled levels.[20] RNA G4s were also targeted in Zika virus-infected cells and shown to mitigate viral levels acting as a roadblock stalling polymerase and ribosome processing.[21] Recently, DNA G4s were predicted at the coding regions of monkeypox genes, and the protein expression was targeted using different G4-binders in a Vaccinia virus strain model.[22] Interestingly, the abovementioned papers used a cationic porphyrin, TMPyP4, a potential inhibitor of human telomerase,[23] to target different G4s structures, indicating its antiviral activity.

In this work, a robust genomic screening in MPXV isolates collected during different outbreaks was performed to map G-rich sequences. Subsequently, we utilized Quadruplex-forming G-rich Sequences (QGRS) Mapper[24] and G4RNA screener[25] to calculate putative G4 folding scores of G-rich sequences from the MPXV genome. A conservation study indicated two unique putative G4 structures disturbed in close-related *Orthopoxvirus*. Using biophysical tools, we further characterized both G-rich sequences to establish that they adopt G4 structures in solution. Finally, we demonstrate the ability of G4s to interact with TMPyP4 in vitro. Overall, our results demonstrate for the first time that the MPXV genome contains G4-forming sequences that could potentially be targeted using TMPyP4 and other G4-interacting drugs to explore therapeutic development avenues.

2 | MATERIALS AND METHODS

2.1 | Genome mapping and sequence conservation analysis

Genome data were collected on the Nucleotide database of NCBI, where all 590 complete MPXV genomes (accessed in August 2022) isolated from different countries and years were assembled for further sequence analysis. All genomes used with their respective NCBI code are available in Supporting Information: Table 1. To assess

the diversity of sequences, a phylogenetic tree using the 590 sequences was done as follows. MPXV genome file was aligned using MAFFT (Multiple Alignment using Fast Fourier Transform)[26] and further assigned to different clades according to differences in query and reference sequences through Nextclade. The maximum-likelihood method was used to construct a phylogenetic tree using IQ-tree[27] and the tree was finally visualized using iTOI v5.[28] A total of 38 sequences were assigned to Clade I, whereas 552 sequences are accommodated in Clade II (Supporting Information: Figure 1). Then, the Putative Hybrid-Quadruplex forming Sequence (PHQS) script performed an initial screening to map G-rich regions in all genomes as previously described[29] according to the following parameters: G-tract size = 2, loop size 1−5, number of g-tracts equal or higher than 4, search range 210 000, bin size 100 nucleotides. The percentage of hits was achieved by dividing the number of times each sequence appeared in the prediction for the number of genomes used (n = 590). Next, recovered sequences were ranked using QGRS mapper,[24] following default parameters, and G4RNA screener[25] based on cGcG (Consecutive G over consecutive C ratio), G4H (G4Hunter), and G4NN (G4 Neural Network) with a defined threshold of cGcG >4.5, G4H >0.9, and G4NN >0.5.

The nucleotide Basic Local Alignment Tool (BLASTn)[30] was used to assess similarities within MPXV sequences against viruses from the *Orthopoxvirus* genus. MPXV selected putative G4-sequences were individually aligned with Smallpox (taxid: 10 255, n = 55), Cowpox (taxid: 10 243, n = 22), Camelpox (taxid: 28 873, n = 9), and Horsepox (taxid: 397 342, n = 3) genomes using BLASTn default parameters. Matching sequences were further realigned using Clustal Omega multiple sequence alignment tool.[31] All genomes used with their respective NCBI code are available in Supporting Information: Table 1.

2.2 | Circular dichroism (CD) spectroscopy

Synthetic lyophilized oligonucleotides were purchased from Alpha DNA. The oligos used in this study are described in Table 1. MP1, MP2 and their respective mutants were dissolved to 20 µM using a G4 buffer (20 mM HEPES, 100 mM KCl, and 0.2 mM EDTA, at pH 7.4). Before data collection, the oligos were heated at 95°C for 5 min and cooled down at room temperature for 30 min. Jasco J-815 spectropolarimeter (Jasco Inc.) was used to collect spectra of all oligos ranging from 220 to 320 nm, using a 1.0 mm cell, 0.1 nm data pitch, with five accumulations and 32 s integration time. A continuous supply of nitrogen gas was provided to avoid water condensation in the cells. All measurements were baseline corrected with G4 buffer and repeated in triplicate.

TABLE 1 Representative codes and sequences for the oligos used in this study.

Oligo	Sequence
MP1	5′-ATTAGGTGGGGGATGGACAA-3′
MP1 mutant	5′-ATTAGGTGAGAGATGGACAA-3′
MP2	5′-GGTAAAGGAGGAAAGGGTGG-3′
MP2 mutant	5′-GATAAAGGAGAAAAAGGTGG-3′
T7 primer	5′-TAATACGACTCACTATAGGG-3′
Telomeric G4	5′-TTAGGGTTAGGGTTAGGGTTAGGG-3′

2.3 | Solution small-angle X-ray scattering (SAXS)

SAXS data were collected using the B21 BioSAXS beamline at the Diamond Light Source, using an Agilent 1200 HPLC connected in line with a specialized flow-cell, as previously described.[32] Samples of wild-type and mutant oligos were concentrated to 150 µM, heated and cooled as described above, and injected into the Shodex KW402.5-4 F, preequilibrated with G4 buffer. About 600 frames, with 3 s exposure were collected. Scattering data were analyzed using the ATSAS suite, version 2.8.[33] We used Chromixs to buffer baseline correct samples peak intensity.[34] Samples' quality check and the radius of gyration (R_g) were assessed by performing a Guinier analysis (q^2 vs. ln(I(q))).[35] The folding of wild-type and mutants were obtained by a dimensionless Kratky plot (qR_g vs. $qR_g{}^2$*I(q)/I(0))[36] and a paired-distribution function (P(r)) provided the real-space R_g and the maximum particle dimension (D_{max}) using GNOM.[37] P(r) plot was the input data to DAMMIN[38] calculates 11 models of each oligo, selecting different seeds for each model although using equal parameters to ensure symmetry. DAMAVER was used to obtain an average model, and DAMFILT yielded a filtered representative structure model.[39]

2.4 | Microscale thermophoresis (MST) studies

MST experiments were done at room temperature using the Nanotemper Technologies Monolith® NT.115 instrument and standard capillaries to measure fluorescence counts, binding affinity, and binding check. For the Thioflavin assay, 5 µM of oligos diluted in G4 buffer and previously heat-cooled (as mentioned above) were incubated with 1 µM of Thioflavin T for 15 min. MST was used to collect initial fluorescence counts. Samples were analyzed in quadruplicate; fluorescence counts were normalized based on telomeric G4 (positive control, sequence in Table 1), and data were statistically analyzed using an unpaired t-test on GraphPad Prism 9.4 software.

A DHX36 construct carrying the N-terminal amino acid residues ranging from 53 to 105 ($DHX36_{53–105}$), containing DNA and RNA G4 interacting motif, was cloned and purified as previously described by our group.[14] The reaction was prepared by mixing 100 nM of 5′ FITC labeled oligonucleotide with $DHX36_{53–105}$ ranging from 0.001 to 17.5 µM diluted in MST buffer (20 mM HEPES, 100 mM KCl, 0.2 mM EDTA, and 0.05% Tween 20, at pH 7.4), and incubated at room temperature for 20 min. Subsequently, binding affinity experiments were performed using medium MST-Power, 50% excitation-power, with data collection on the cold region at 0 s and the hot region at 5 s.

Another binding affinity experiment tested the interaction between TMPyP4 within G4-forming and mutant oligos following the same methodology described above. TMPyP4 was acquired from Sigma Aldrich (CAS number 36951-72-1), diluted from 1.1 to 0.0003 μM and further incubated at room temperature for 20 min with 100 nM of 5′ FITC labeled oligonucleotides. Three independent replicates from $DHX36_{53–105}$ and TMPyP4 binding affinity were submitted to data collection and analyzed on MO Affinity Analysis software (version 2.1.3). The software uses thermophoresis-based fluorescence changes to calculate the binding affinity, K_d. GraphPad Prism 9.4 software was used to plot curves.

For the competitive assay, 100 nM of G4-forming oligonucleotides were mixed first with 500 nM of TMPyP4 in MST buffer; the reaction was prepared in four tubes and incubated at room temperature for 20 min. Then, 500 nM of $DHX36_{53–105}$ was added to two tubes, whereas the other two were filled with MST buffer. In a different set, the oligonucleotides were first incubated with 500 nM of $DHX36_{53–105}$ for 30 min, and then half of them were incubated with 500 nM of TMPyP4 for additional 30 min. The experiment was done in duplicate with four reactions in each set, totaling eight points per condition tested. Data was collected via an MST binding check that ran using medium MST power, 50% excitation power, on the cold region at 0 s and the hot region at 5 s at room temperature. Fluorescence changes due to thermophoresis were recorded and normalized using MO Affinity Analysis software (version 2.1.3), and the graph was plotted using GraphPad Prism 9.4 software.

2.5 | MPXV gene expression experiments

The MPXV genes A27L and A50R were cloned into a mammalian expression vector, pcDNA 3.1(+), and expressed linked with red-fluorescence protein (RFP) as a reporter. The A27L and A50R sequences were retrieved from the *Monkeypox* reference sequence (NC_063383) available in the NCBI database and synthesized and purchased from Biomatik. An RFP-expressing plasmid (#26720; Addgene) was used as a negative control. The plasmids were transformed into *Escherichia coli* DH5α and selected on ampicillin-resistant agar plates. Individual colonies were inoculated in LB media and plasmids were purified using the GeneJET Plasmid Maxiprep Kit (Thermo Fisher Scientific) according to the manufacturer's instructions. HEK293 cells were seeded in 35 mm petri dishes (2.0×10^5 cells/dish). Once the cells reached ~80% confluence, they were transfected with 5 μg of A27L, A50R, or RFP_{ctrl} plasmids per dish using Lipofectamine™ 3000 Transfection Reagent (Invitrogen) following the manufacturer's protocol. After 24 h of transfection, cells were treated with 0, 10, 15, or 20 μM of TMPyP4 and kept in the dark for an additional 20 h. The cells were then imaged using an Olympus FV1200 confocal microscope with brightfield microscopy and RFP filter, using excitation 488 nm and emission 561 nm. Images were collected and analyzed using FV1200 Olympus software. All microscope images were quantitatively analyzed on ImageJ software.

3 | RESULTS

3.1 | Predicted G4 sequences are predominantly localized in the right terminal region and are MPXV exclusive

We employed a computational screening in 590 genome isolates across the globe using the PHQS script exploring G-rich sequences following a pattern of $(G \geq 2, 1 \leq N \geq 5)_{4\leq}$, where G is guanines, and N is the number of nucleotides held in the loop between two G-tracts. Eleven putative G-rich sequences were retrieved, with 7 identified in all 590 genomes (100% hits), 3 in 588 genomes (99%), and 1 only detected in 24 genomes (4%) (Figure 1A). MPXV genome carries left and right terminal regions that comprise noncoding ITR. One putative sequence was predicted on the Left terminal region, whereas 8 sequences are concentrated at the right terminal region. Also, a central conserved region contains 2 putative sequences in the middle of the genome. Using the DRC 2008 isolate as a reference (GenBank accession KP849469), a corresponding gene for each putative sequence was identified. All predicted sequences are localized in the coding region, and their respective protein code is available in Figure 1A. The nucleotide length varies from 15 to 48, but the G-score was calculated using the minimal predicted G4. G-scores above the threshold are presented in bold green, whereas below the threshold are presented in red. QGRS Mapper identified 4 putative G4-sequences (threshold ≥19) while Ghunter (threshold ≥0.9), cGcG (threshold ≥4.5), and G4NN (threshold ≥0.5) detected 7, 10, and 7 sequences, respectively. Collectively analyzing the predicted G-score along with conservation hits across MPXV strains, G4-sequences related to the genes A27L and A50R were selected for further studies and referred to as MP1 and MP2, respectively.

A local alignment was conducted to analyze the conservation of selected putative G4-sequences against disease-associated members of the *Orthopoxvirus* genus (Figure 1B). MP1 and MP2 were aligned with Smallpox ($n = 55$), Cowpox ($n = 22$), Camelpox ($n = 9$), and Horsepox ($n = 3$), and their corresponding sequences are presented in Figure 1B. Sequence alignment for MP1 demonstrates 85% similarity, with three nucleotide gaps in the center. Regarding MP2, Smallpox, Horsepox, and Cowpox contain a cytosine residue instead of a guanine residue in the MPXV genome, whereas Camelpox differs from MPXV by substituting double guanine residues with thymidine and cytosine residues. Cowpox has one genome with 100% similarity with MP1 (DQ437593.1) and four with 100% similarity with MP2 (KY549143.2, KY369926.1, HQ407377.1, X94355.2). Interestingly all variations were observed to be substituting guanine

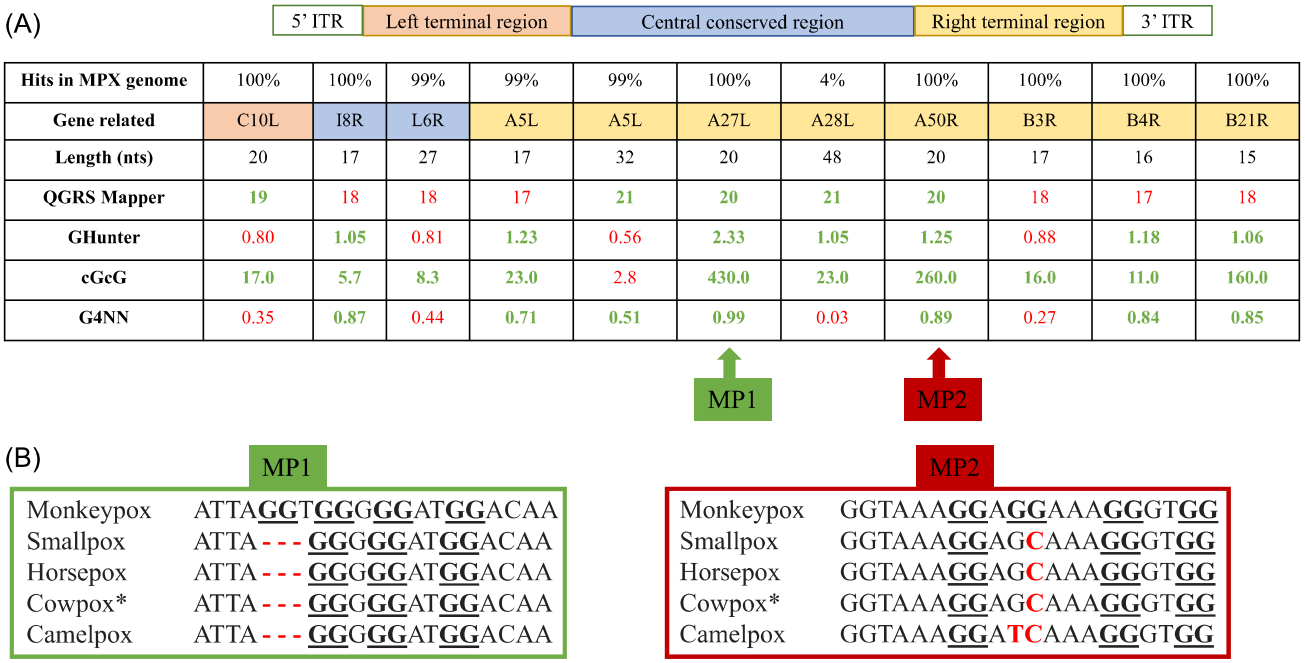

Hits in MPX genome	100%	100%	99%	99%	99%	100%	4%	100%	100%	100%	100%
Gene related	C10L	I8R	L6R	A5L	A5L	A27L	A28L	A50R	B3R	B4R	B21R
Length (nts)	20	17	27	17	32	20	48	20	17	16	15
QGRS Mapper	19	18	18	17	21	20	21	20	18	17	18
GHunter	0.80	1.05	0.81	1.23	0.56	2.33	1.05	1.25	0.88	1.18	1.06
cGcG	17.0	5.7	8.3	23.0	2.8	430.0	23.0	260.0	16.0	11.0	160.0
G4NN	0.35	0.87	0.44	0.71	0.51	0.99	0.03	0.89	0.27	0.84	0.85

FIGURE 1 Mapping putative quadruplexes in MPXV genome followed by a conservation analysis. (A) Representative genome of the Poxviridae family flanked by 5' and 3' inverted terminal repeats (ITR) followed by a left terminal region (orange), central conserved region (blue), and right terminal region (yellow). Gene localization was individually represented in each column following the color code used before to demonstrate genomic position. Then, the nucleotide length of putative sequences and predicted *G*-score for each are presented in the subsequent rows. Numbers displayed in bold green are above the defined threshold, whereas red numbers correspond to *G*-scores under the threshold. (B) Conservation analysis of MP1 (green square) and MP2 (red square) sequences against human disease-related Orthopoxvirus. *Only Cowpox has one genome with 100% similarity with MP1 and four with 100% similarity with MP2. MPXV, monkeypox virus.

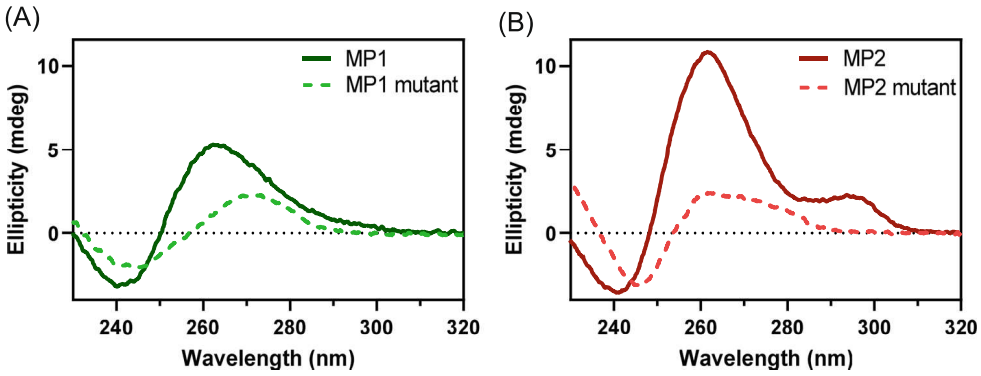

FIGURE 2 Circular dichroism (CD) spectroscopy reveals that MPXV oligos fold in a parallel topology. (A) and (B) CD spectroscopy profiles of MPXV G4 MP1 (continuous green line) and MP2 (continuous red line), as well as MP1 mutant (dashed green line) and MP2 mutant (dashed red line), demonstrate that a single mutation in MP1 and MP2 G4 oligos leads to a change in G4 secondary structures. MPXV, monkeypox virus.

residue disrupting G-tracts, negatively impacting the putative G4-sequence score.

3.2 | Biophysical evaluation of G4 formation

To assess the ability of MP1 and MP2 to fold into a G4, two 20-mer wild-types (MP1 and MP2) oligos were synthesized and evaluated using biophysical methods (Table 1). Additionally, MP1 and MP2 mutants were also designed to disrupt the G4 second quartet by replacing two guanines with adenines. Immediately before performing experiments, all the oligonucleotides were heated at 95°C for 5 min and cooled down at room temperature for at least 15 min. CD spectroscopy was used to investigate G4 folding and topology in the presence of potassium ions (Figure 2A). A noticeable positive peak at around 263 nm and a deep negative peak at about 243 nm were observed for MP1 (left plot, continuous green line) and MP2 (right plot, continuous red

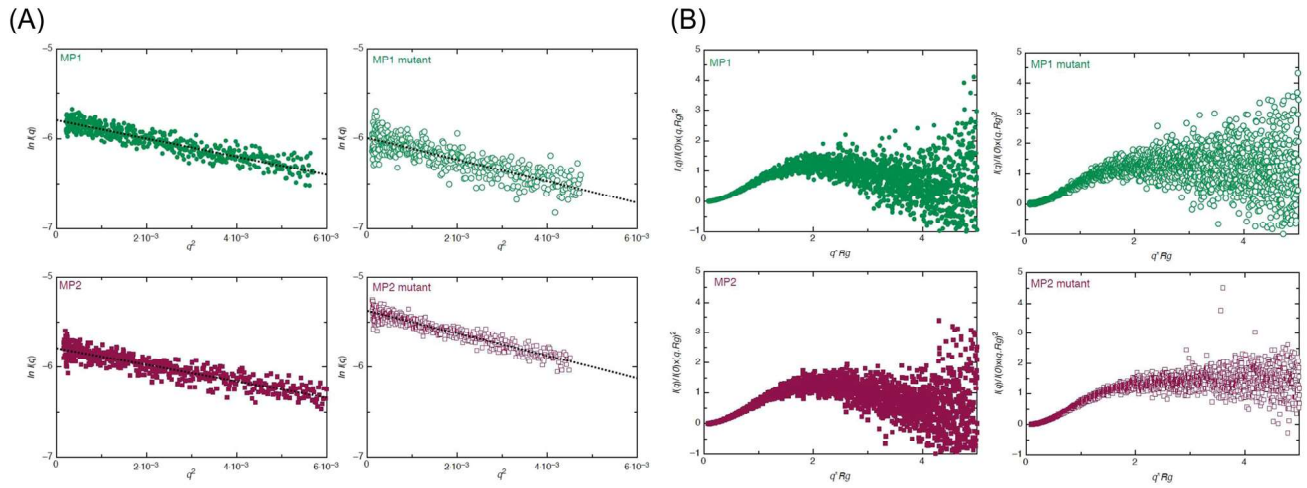

FIGURE 3 Guinier and Kratky's plots indicate that oligomers are free of aggregation and properly folded in solution. (A) A liner Guinier (Ln (I,q)) vs. q^2) region indicates that all samples are pure and aggregation-free. (B) Dimensionless Kratky plots $(I(q)/I(0)*(q*R_g)^2$ vs. $q*R_g$) suggest that both wild-type and mutants are folded and appropriate for low-resolution structure determination. Also, an effect of a single mutation for MP1 and MP2 G4 oligo is evident by the differences between dimensionless Kratky plots for wild-type and mutants. MP1, green colored circle; MP1 mutant, green blank circle; MP2, red colored square; and MP2 mutant, red blank square.

TABLE 2 Analysis of small-angle X-ray scattering data for MP1, MP2, and their mutants.

Parameters	MP1	MP1 mutant	MP2	MP2 mutant
Sequence molecular weight ($gmol^{-1}$)	6286.2	6254.2	6360.2	6312.2
Guinier I(0)	$0.0031 \pm 1.7 \times 10^{-5}$	$0.0025 \pm 2 \times 10^{-5}$	$0.0031 \pm 1.6 \times 10^{-5}$	$0.0047 \pm 2 \times 10^{-5}$
Guinier R_g (Å)	17.18 ± 0.20	18.90 ± 0.30	16.31 ± 0.17	19.38 ± 0.16
$q.R_g$ range	0.25–1.30	0.20–1.30	0.20–1.30	0.24–1.30
P(r) I(0)	$0.0030 \pm 1.1 \times 10^{-5}$	$0.0024 \pm 1.5 \times 10^{-5}$	$0.0030 \pm 1.6 \times 10^{-5}$	$0.0046 \pm 1.6 \times 10^{-5}$
P(r) R_g(Å)	16.18 ± 0.05	18. 28 ± 0.10	15.54 ± 0.05	19.55 ± 0.10
D_{max} (Å)	44	55	45	59
χ^2	1.10	1.05	1.18	1.08
NSD	0.64 ± 0.02	0.53 ± 0.01	0.66 ± 0.02	0.57 ± 0.01

Abbreviation: NSD, normalized spatial discrepancy.

line), suggesting that both oligonucleotides can fold into a G4 structure in a buffer containing potassium ions and adopt a parallel topology.[40] Inversely, the MP1 mutant (left plot, dashed green line) showed a shift to the right with a positive peak around 272 nm and a negative close to 245 nm. MP2 also had a minor right change in the negative peak to around 248 nm, and a broad positive peak could be seen from 260 until 275 nm. Both mutant patterns are atypical to any well-known G4 topology, suggesting that these oligos cannot fold into a G4 structure.

Further, low-resolution structures were determined to visualize differences in wild-type G4-forming oligos compared to their respective mutants using SAXS. The merged intensity data (Supporting Information: Figure 2) and Guinier analysis (Figure 3A) demonstrate that our samples are pure and monodisperse. The linearity observed in the Guinier plots indicates an aggregation-free solution and allows the calculation of R_g using low angle region, presented in Table 2 as Guinier R_g (Å). An elongated structure could be observed in both mutants with R_g of approximately 19 Å, whereas MP1 and MP2 are more compacted, with 17.18 and 16.31 Å, respectively. Next, we performed dimensionless Kratky and P(r) function analysis to further gain insights into oligos' folding, conformation, and compactness states.[41] The dimensionless Kratky plot suggested that wild-type oligos exhibit comparable folding states, reasonably distinct from those steady plateau displayed by mutants but indicating that all oligos are folded and are appropriate for low-resolution three-dimensional structure determination (Figure 3B). The P(r) plot was derived from indirect Fourier transformations to

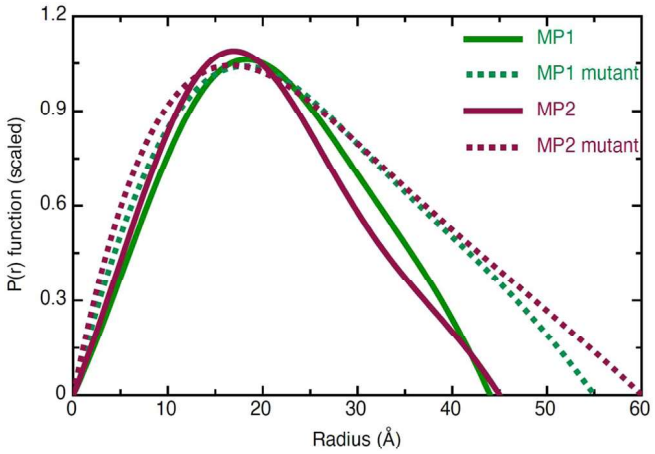

FIGURE 4 Normalized pair distribution function of MPXV oligomers. P(r) versus radial distance plot indicates that as expected, both wild-type G4s have similar dimensions and are compact, whereas, both mutants are extended in solution. MP1 (continuous red line) and MP2 (continuous green line) assume a compact and solid structure, while MP1 mutant (red dashed line) and MP2 mutant (green dashed line) fold into an elongated structure. G4s, G-quadruplexes; MPXV, monkeypox virus.

convert reciprocal information on the Guinier plot into a real-space electron paired distribution.[42] Oligos' R_g was calculated in real-space (P(r) R_g(Å), in Table 2) and corresponded to those achieved by the Guinier plot, with slight differences in G4-forming oligos where real-space R_g are 16.18 and 15.54 Å, presented with about 1 Å unit more in Guinier. Additionally, the Gaussian distribution observed in the P(r) plot indicates that both mutants have a compacted structure with equivalent maximum particle dimension, yet the mutants are displayed in an elongated structure with D_{max} around 55 and 59 Å for MP1 and MP2, respectively (Figure 4).

DAMMIN was used to generate 11 low-resolution structures of wild-type and mutant oligos. The goodness of fitting (χ^2) within all generated models is presented in Table 2 and statistically indicates a favorable agreement for all 4 oligomers. Consecutively, the normalized spatial discrepancy (NSD) was calculated to verify the agreement within low-resolution structures calculated using DAMMIN. NSD values, presented in Table 2, indicate that in each case, all DAMMIN-derived structures are in good agreement with each other. Consequently, we present averaged and filtered low-resolution

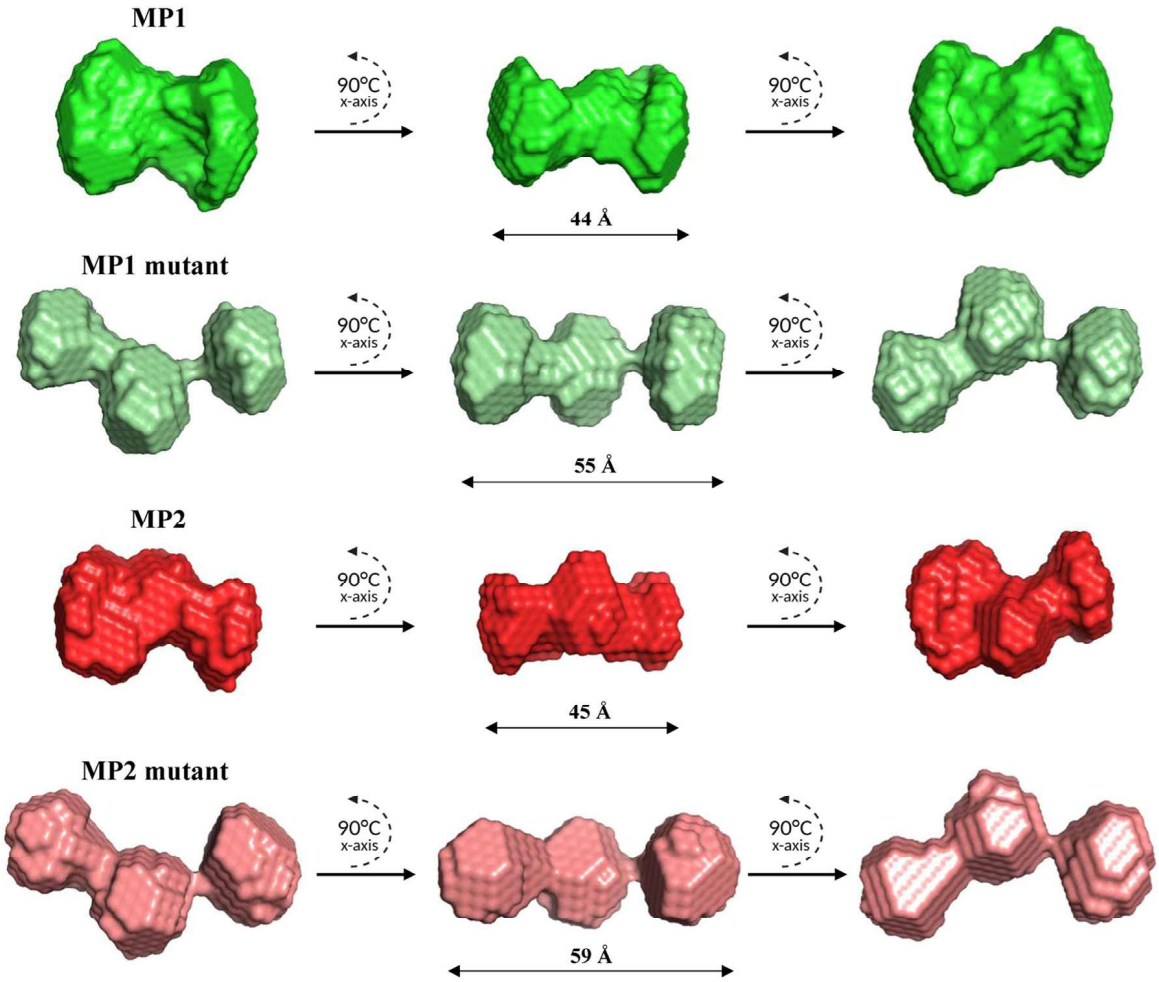

FIGURE 5 Low-resolution three-dimensional structures of MPXV oligos. DAMFILT filtered representative models with two consecutive 90°C rotations along their *x*-axis. Horizontal arrows represent their D_{max} obtained from the pair-distribution function. As expected, MP1 (red) and MP2 (green) have a compacted quasi-globular shape, whereas MP1 mutant (pale green) and MP2 mutant (dark salmon) displayed an elongated structure that is very similar to each other. MPXV, monkeypox virus.

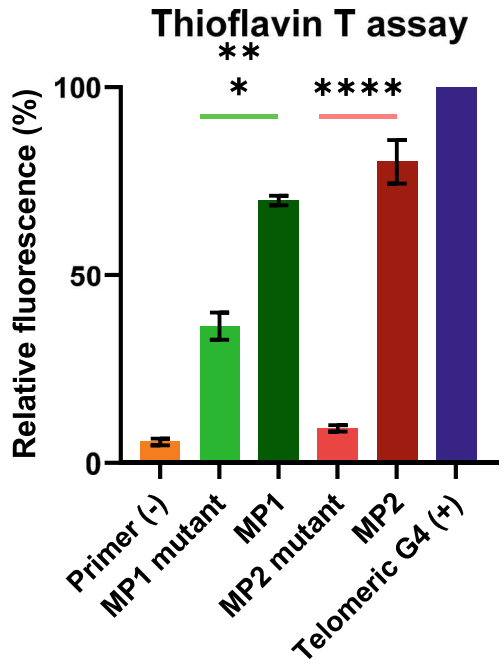

FIGURE 6 Thioflavin T assay indicates MPXV G4s folding by stacking two tetrads. Thioflavin T assay measures the relative fluorescence of MPXV oligos, demonstrating that MP1 and MP2 present a high amount of relative fluorescence, compared to non-G4 forming primers (negative control) or mutants. Relative values were calculated based on well-established Telomeric G4 (blue bar) as a positive control. G4s, G-quadruplexes; MPXV, monkeypox virus.

structures for each oligo in Figure 5. Altogether, the low-resolution structures emphasize that mutants adopt comparable elongated structures while G4-forming sequences fold into dense and quasi-globular structures.

3.3 | Parallel G4s interact with quadruplexes-binding partners

Next, we determined the ability of the oligomers to fold in solution and be recognized by well-established G4-binding partners. As previously demonstrated, Thioflavin T (ThT) recognizes telomeric G4 DNA with high affinity.[43] Therefore, relative fluorescence was calculated using Telomeric G4 as 100% fluorescence counts; T7 primer was used as a non-G4 forming sequence. MP1 has an average relative fluorescence of 70% when compared to Telomeric G4, while MP1 mutant had a signal of around 35% (Figure 6). Also, it is perceptible that MP2 had a fluorescence signal of around 80% and its relative mutant a slightly superior intensity than T7 primer, at around 10%. An unpaired *t*-test statistically supports a significant distinction between MP1 and its mutant with a *p*-value = 0.001 and between MP2 and MP2 mutant, which the *p*-value < 0.001. Altogether, these results indicate that ThT is a suitable sensor for detecting MP1 and MP2 in solution, emphasizing their ability to fold into G4.

Furthermore, we also asked if $DHX36_{53–105}$, a member of the DEAH-box helicase family described to interact with G4 structures, can recognize MPXV G4s.[14,44,45] The MST binding assays of MPXV G4s with the G4 interacting N-terminal motif of $DHX36_{53–105}$ suggested the K_d of 44.0 ± 1.8 nM for MP1 (continuous green line) and 611.9 ± 234.3 nM for MP2 (continuous red line). Conversely, the binding affinities of mutants for the $DHX36_{53–105}$ were determined to be in a micromolar range (Figure 7A). Mutants from MP1 (green dashed line) and MP2 (red dashed line) interact with $DHX36_{53–105}$ with a binding affinity of 16 354.6 ± 1632.7 and 11 953 ± 920.7 nM, respectively.

After utilizing a G4 interacting fluorescence sensor and $DHX36_{53–105}$ protein, we assessed if TMPyP4, a cationic porphyrin chemical that targets G4 structures, also recognizes MPXV G4s.[20,46] We used MST to determine that MP1 and MP2 bind to TMPyP4 with K_d of 182.3 ± 14.3 and 180.9 ± 22.6 nM, respectively (Figure 7B and Table 3). MP1 mutant also interacts with TMPyP4 in a nanomolar range (612.3 ± 47.6 nM), although interaction strength is around 3.3 times weaker than MP1. Furthermore, the MP2 mutant interacts with TMPyP4 in a micromolar range (4324.7 ± 199.2 nM), suggesting a binding event only starts at exceptionally high concentrations.

3.4 | TMPyP4 outcompetes with $DHX36_{53–105}$ for MPXV G4 binding site

A competitive assay was performed to understand if TMPyP4 can recognize G4 structures in the presence of another intrinsic cellular partner, such as $DHX36_{53–105}$. Using MST, G4-forming oligos were incubated with TMPyP4 (Figure 8, black circles), followed by the determination of the normalized fluorescence for MP1 and MP2. Our assays indicated the fluorescence units of 1050 for MP1 and 975 for MP2 (Figure 8A,B). After adding an equal concentration of $DHX36_{53–105}$ to each reaction tube, no statistically significant differences were observed for both MP1 and MP2 (green and red circles in Figure 8). Inversely, G4-forming oligos were first incubated with $DHX36_{53–105}$ (black triangles in Figure 8) and then supplemented with an equal amount of TMPyP4. A significant statistical difference ($p < 0.0001$) was observed for MP1 (green triangles, Figure 8A) and MP2 (green triangles, Figure 8B) using an unpaired *t*-test. This competitive assay and interaction experiments strongly suggest that TMPyP4 outcompetes and stabilizes G4 structures, whether binding to an intrinsic cellular partner or not.

3.5 | TMPyP4 treatment downregulates expression of MPXV A27L and A50R genes

To determine whether TMPyP4 stabilization of G4s can modulate MPXV genes, we designed a gene expression system for MPXV A27L and A50R genes, which carry MP1 and MP2, respectively.

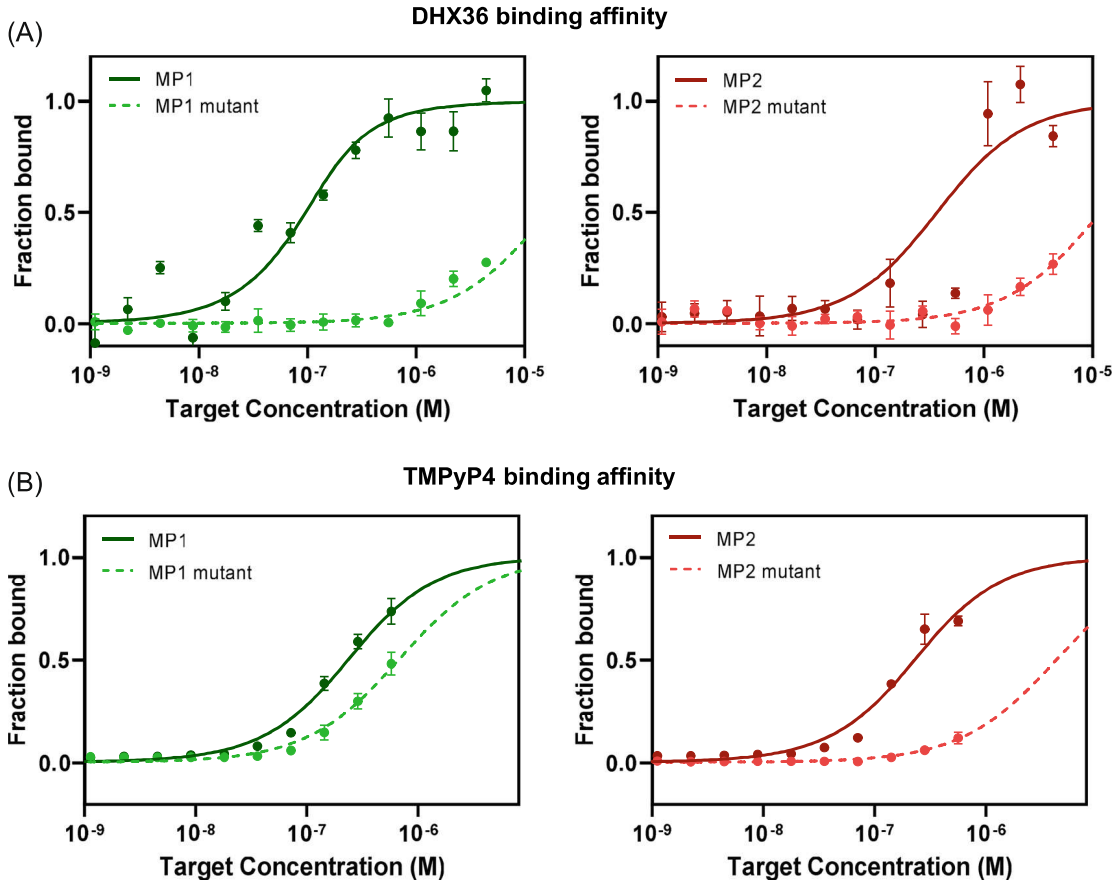

FIGURE 7 Assessment of binding affinity using MST between MPXV G4s and G4-binding partners. We determined the affinity of (A) $DHX36_{53–105}$ and (B) TMPyP4 with MPXV oligos. MST data for MP1 (continuous green line) and MP1 mutant (dashed green line) are presented on the left side, and for MP2 (continuous red line) and MP2 mutant (dashed red line) on the right side. FITC fluorescent oligos were constantly added to the reaction capillaries while a varied concentration of $DHX36_{53–105}$ and TMPyP4 was tested. Dissociation constants (K_d) were calculated based on a curve fitting and are presented in Table 2. The binding curves demonstrate that both $DHX36_{53–105}$ and TMPyP4 interact with nanomolar affinity to MP1 and MP2, compared to mutants. G4s, G-quadruplexes; MPXV, monkeypox virus; MST, microscale thermophoresis.

TABLE 3 The dissociation constant (K_d) calculated using MST for MPXV G4's and their respective mutants interaction with $DHX36_{53–105}$ and TMPyP4.

	DHX36	TMPyP4
MP1	44.0 ± 1.8 nM	182.3 ± 14.3 nM
MP1 mutant	16 354.6 ± 1632.7 nM	612.3 ± 47.6 nM
MP2	611.9 ± 234.3 nM	180.9 ± 22.6 nM
MP2 mutant	11 953.0 ± 920.7 nM	4324.7 ± 199.2 nM

Abbreviations: MPXV, monkeypox virus; MST, microscale thermophoresis.

MPXV gene expression was tracked through the fluorescence reporter RFP in a cellular system, as demonstrated in the schematic Figure 9A. A plasmid expressing RFP (RFP_{ctrl}) was used as a negative control upon TMPyP4 treatment, as no G4 has been reported on the RFP sequence. As expected, RFP expression in RFP_{ctrl} remained basically unaltered after treatment with TMPyP4 at different concentrations 10, 15, and 20 μM (Figure 9B, top panel). A trivial decrease was observed after treatment with 20 μM of the porphyrin (Supporting Information: Figure 4). However, treatment of MPXV genes caused a substantial reduction of RFP expression starting at 10 μM of the TMPyP4. While A27L gene expression (Figure 9B, middle panel) was decreased by about 25% upon treatment with 10 μM of TMPyP4, a substantial reduction of 50% was observed at higher concentrations (Supporting Information: Figure 3). A50R-RFP expression was observed through tiny fluorescence dots (Figure 9B, bottom panel), in a different pattern than was noticed in RFP_{ctrl} and A27L. However, TMPyP4 treatment was effective in constraining A50R gene expression at similar concentrations to those observed in A27L (Supporting Information: Figure 3). Additionally, bright microscope images demonstrated that cells are viable and healthy after treatment, suggesting nontoxic activity at the tested concentrations (Supporting Information: Figure 4).

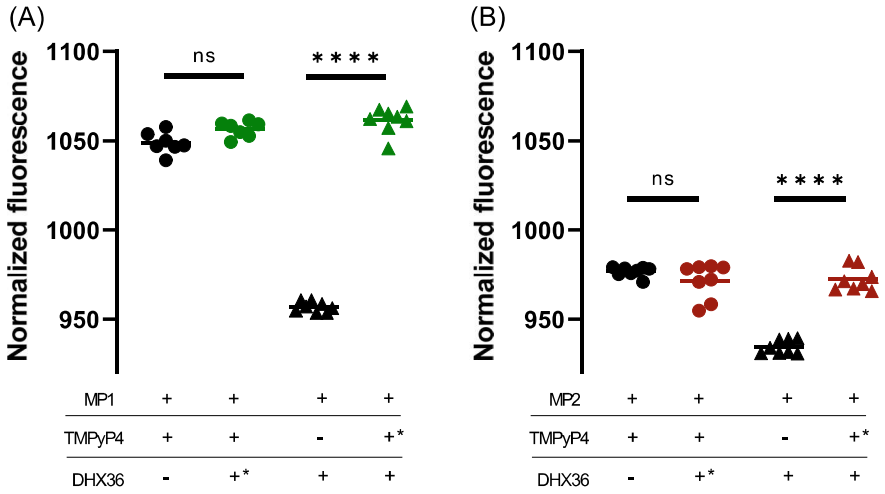

FIGURE 8 G4 binding partners competitive assay within MPXV G4s assessed using MST. (A) MP1 and (B) MP2 were first incubated with TMPyP4 in the absence of $DHX36_{53-105}$ (black circles). In a different reaction, an equal concentration of $DHX36_{53-105}$ was added to the oligos and TMPyP4 mixture (MP1—green circles in [A] and MP2—red circles in [B]). Similarly, both oligos were incubated in the absence of TMPyP4 (black triangles) followed by an equivalent reaction with equal concentrations of TMPyP4 (MP1—green triangles in [A] and MP2—red triangles in [B]). These experiments demonstrate that MP1 and MP2 can be recognized by TMPyP4, even though they are bound to $DHX36_{53-105}$. On the other hand, if MP1 and MP2 are already bound to TMPyP4, they cannot interact with $DHX36_{53-105}$. Thus, these data highlight that TMPyP4 is able to interact with and stabilize MPXV G4s in the presence of host G4-interacting proteins. *Indicates the component that was secondly added to the reaction mixture. G4s, G-quadruplexes; MPXV, monkeypox virus; MST, microscale thermophoresis.

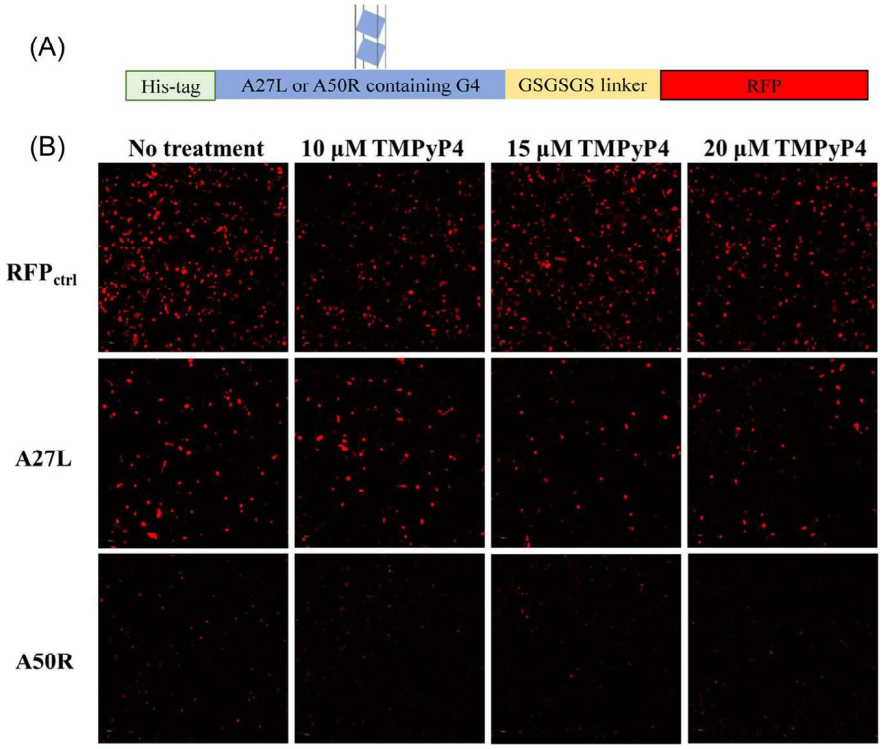

FIGURE 9 TMPyP4 treatment reduced expression of MKPX A27L and A50R genes in HEK293 cells. (A) Schematic representation of construct designing. All the constructs were designed in pcDNA 3.1(+) plasmid with a His-tag coding region (in green), followed by the specific with containing the G4 or the non-G4 control (in blue), and glycine-serine rich linker (in yellow) and the RFP-coding sequence (in red). (B) Cells transfected with RFP-expressing plasmid were treated with 0, 10, 15, and 20 µM of TMPyP4 (top panel) and used as control, while cells transfected with MPXV genes A27L and A50R, fusioned with RFP, were also treated with TMPyP4 and could be observed at middle and bottom panel, respectively. Porphyrin treatment clearly is inefficient in reducing RFP expression at the top panel. However, in A27L and A50R infected cells treated with 15 and 20 µM of TMPyP4, a substantial reduction in overall fluorescence could be noticed after stabilization of G4s when compared to their respective untreated cells. Cells were observed at a confocal microscope using RFP excitation and emission at a x10 magnification. G4s, G-quadruplexes; MPXV, monkeypox virus; RFP, red-fluorescence protein.

4 | DISCUSSION

Structural insights and characteristics in the MPXV genome are poorly understood. Most of what is known were either achieved by sequence similarity with close-related Poxvirus or old literature reports that evaluate particular genomic organization features.[47–49] For the first time, a detailed mapping within more than 500 MPXV genomes from different outbreaks across the globe pinpointed various G-rich sequences that potentially fold into a G4 in solution. As the first step of bioinformatic screening, a genomic analysis using the PHQS was performed. PHQS was primarily designed to determine the increasing prevalence and abundance of hybrid-quadruplex over intramolecular G4s by analyzing the transcription start site of several genomes.[29] However, we used the PHQS script solely to identify G-rich sequences throughout MPXV genomes regardless of inter- or intramolecular G4. An in-depth score-based prediction was subsequently used to classify putative G-rich sequences.

Collected putative G4-sequences ranged in nucleotide length from 15 to 48-mer (Figure 1A). However, G4-predictive scores were calculated by counting only the minimal sequence comprising the four G-tracts, considering that additional nucleotides could underestimate the score. QGRS Mapper uses retrieved nucleotide sequence information to generate a G-score based on loop size, considering the size and equivalent distribution of nucleotides on the loops.[24] The total number of tetrads also impacts the G-score; where more tetrads are formed, a more stable G4 structure can be formed. Even though the QGRS software does not provide a baseline score, a previously published paper established a threshold of 19 residues and demonstrated that all predicted oligos above the score folded into a G4 in vitro.[15] Alternatively, the G4RNA screener uses a machine learning approach combined with an experimentally validated G4 set to provide a sequence-based G-score using three objective analyses: cGcG, G4Hunter, and G4NNN.[25] cGcG ratio and G4Hunter score system are based on the competitive rates of Watson-Crick and Hoogsteen-based structures, where excessive cytosine over guanine can hinder G4 formation.[25,50] Otherwise, G4NN uses an artificial neural network to evaluate similitudes among input sequences within an experimental G4 database.[25] Although both QGRS and G4RNA screener were designed for RNA G4s, G4Hunter was modeled to analyze DNA G4s with high accuracy.[51] Also, the loop size and distribution, as well as the number of G-tracts for canonical G4s, are equivalent for DNA and RNA molecules, which does not impair the scoring system. Previous work had also predicted DNA G4s using the QGRS Mapper scoring approach.[52]

Putative G4-sequences were pinpointed in different protein-coding regions of the MPXV genome, although only the Right terminal region possesses 8 out of 7 sequences. MP1 was identified in the antisense strand of the A27L coding gene. A27L possesses a reverse open-reading frame gene that encodes 1 of the viral A-type inclusion proteins frequently targeted for viral neutralization[53] and is responsible for environmental protection during *Orthopoxvirus* infections.[54] Meanwhile, MP2 was positioned inside the gene A50R that encodes the ATP-dependent DNA ligase, responsible for repairing nicked DNA duplexes in Vaccinia virus[55] with mutations associated in new lineages of MPXV isolates.[56] Furthermore, conservation studies analyzing disease-related *Orthopoxvirus* genomes against MPXV G-rich sequences showed that putative G4s are MPXV-exclusive (Figure 1B). The subtle variations observed in nucleotide arrangement impair the formation of G4 in other disease-related *Orthopoxviruses* once an essential G-tract is disrupted. Thus, the localization of G4 sequences in important coding sites and the strong conservation and exclusiveness collectively indicate that these structures may modulate either viral environmental protection or replication exclusively during MPXV infections.

CD spectroscopy has been established as a primary biophysical method to assess G4 folding in solution and to evaluate the topology of G4s by comparing different spectral profiles.[40] CD analysis of both MP1 and MP2 demonstrate their ability to fold in solution and assume a parallel topology compared to the mutant oligos (Figure 2A). Guinier plots also indicate that wild-type and mutants can fold in solution without aggregation (Figure 3A). Biophysical characterization using SAXS has been routinely used in our lab to characterize long noncoding RNA structures[42] but also to visualize small DNA structures that fold into quadruplexes. Using a 23-mer oligo, our group demonstrated structural differences in a wild-type Hepatitis B virus (HBV) quadruplex when single guanosine is replaced by adenines.[14] Interestingly, the Kratky plot (Figure 3B) and the pair-distribution function (Figure 4) are reasonably similar, with an almost bell-shaped curve when comparing wild-type quadruplexes. Additionally, MPXV G4s have a D_{max} of 44 and 45 Å, which is consistent with HBV quadruplex, whereas mutants' maximum distance is near 60 Å (Table 2). MP1 mutant showed a distinct profile with a slightly reduced D_{max}, 55 Å, exhibiting a slightly compacted structure but still significantly different than wild types. The three-dimensional low-resolution structures clearly represent the abovementioned differences and provide evidence of quadruplex folding in solution (Figure 5).

Biophysical characterization is consistent with MP1 and MP2 interaction with G4-binding partners. ThT was shown to serve as a fluorescence sensor for RNA[57] and DNA G4s[43] by stacking into G-tetrad and stabilizing the K^+ induced G4s. A considerable variation (about 20% −30%) in the relative fluorescence among Telomeric and G4-forming oligos was noticed upon their interaction with ThT, which could be influenced by the number of tetrads (Figure 6). ThT stacks to the tetrads and the Telomeric G4 is formed by three tetrads, while MP oligos are formed by two. Also, the heightened fluorescence intensity for MP1 mutant indicates its ability to form one tetrad and therefore had higher than basal fluorescence counts, coherent with the somewhat compacted structure obtained by SAXS. $DHX36_{53–105}$ is an ATP-dependent helicase well-known to bind via the N-terminal region to G4 containing parallel topologies with high affinity and unwind them.[14,44,45] $DHX36_{53–105}$-specific motif (DSM) localized in the N-terminal portion is essential in G4 recognition,[58] and several factors like the number of G-tracts, stereochemistry and loop size have been shown to alter binding affinity.[59] MST studies have shown that MP1 and MP2 interact with the N-terminal region of $DHX36_{53–105}$ in a comparable nanomolar range to previously reported DNA G4s structures (Figure 7A).[14,58] The difference in binding affinity between MP1 and MP2 could be explained

by the difference in loop size and distribution; while MP1 has a smaller and most equally distributed loop, MP2 has a sizeable central loop and only one nucleotide in the side loops.

To investigate a potential therapeutic application of targeting MP1 and MP2 structures in a cellular system, interaction with TMPyP4 was also estimated. Besides targeting G4 structures in solution and in vivo, TMPyP4 has been described to stabilize DNA G4 structures and inhibit polymerase progression,[20] stall ribosomes on RNA G_4C_2 repeats[46] and unfold an extremely stable RNA G4 present in mRNA to enhance protein translation.[60] Figure 7B demonstrates that MP1 and MP2 interact with TMPyP4 with subnanomolar affinities at a similar range compared to mutant oligos. Similarly observed in the Thioflavin T assay, the MP1 mutant interacted with TMPyP4, indicating its ability to fold into one solely tetrad and leading to the speculation that TMPyP4 preferentially associates with tetrads instead of loops in the G4 structure. In addition, it was previously revealed that TMPyP4 could recognize the DNA G4 structures simultaneously when associated with intrinsic cellular partners, such as $DHX36_{53–105}$ (Figure 8). Contrarily, $DHX36_{53–105}$ could not recognize or compete with G4 binding sites when TMPyP4 is previously associated. Previous literature reported TMPyP4 as an alternative antiviral against Herpes Simplex Virus-1,[20] Zika,[21] Ebola virus,[19] and monkeypox[22] by stabilizing G4 structures and, consequently, inhibiting either transcription or translational events critical to viral replication. The porphyrin concentrations used in the aforementioned studies were similar to the range we used (Figure 9), and cell viability was equally assessed in all of them, demonstrating that concentrations above 25 μM could cause a significant reduction in cellular viability. TMPyP4 treatment demonstrated a remarkable effect in reducing MPXV gene expression without leading to complete inhibition of protein translation. A27L and A50R encode critical proteins for viral survival and protection and are frequently targeted for vaccine development in similar viruses. Consequently, the robust interaction within TMPyP4 and MPXV G4s suggests a promising therapeutic avenue to explore further in a context of a cellular viral infection.

5 | CONCLUSION

In summary, our work provides a deep genomic-scale screening in MPXV isolates to identify G-rich sequences that potentially fold into G4 structures. Sequence similarities and conservation studies demonstrate that two putative G4s are conserved across various outbreak isolates and are MPXV-exclusive. A robust biophysical and biochemical characterization provides evidence that DNA G4s fold in solution, assuming a parallel topology. While this work has shown that the MPXV genome holds two DNA G4s that tightly interact with ThT and $DHX36_{53–105}$ in vitro, additional work is required to elucidate the biological significance of those structures using virology assays. This work also demonstrates an interaction between MPXV quadruplexes and the cationic porphyrin TMPyP4, and treatment with TMPyP4 substantially reduced gene expression of MPXV's important protein. TMPyP4 need to be further validated as an alternative therapeutic approach in a context of a MPXV-infected cells to assess their antiviral activity. Several G4-binding chemicals have been explored within antiviral activity, such as Braco-19 and Pyridostatin (PDS), which could be further explored in MPXV G4s. Finally, our work provides background to the further development of new therapeutics that target MPXV-specific structures.

AUTHOR CONTRIBUTIONS

Higor Sette Pereira and Trushar R. Patel conceptualized the project. Higor Sette Pereira and Darren L. Gemmill performed biophysical and biochemical experiments, analyzed data, and prepared figures. Gunjan Vasudeva performed alignment and phylogenetic analysis and prepared the figure. Higor Sette Pereira and M. Quadir Siddiqui performed cell biology and microscopy experiments, analyzed data, and prepared figures. Higor Sette Pereira wrote the initial draft of the manuscript that was reviewed and edited by all authors. Trushar R. Patel helped with data analysis and supervised work and secured funding.

ACKNOWLEDGMENTS

H. S. P. is supported partly by NSERC CREATE Postdoctoral Fellowship and Canada Research Chair support to TRP. D. L. G. is supported by the NSERC Discovery grant to TRP (RPGIN 2022–03391). This work was also supported by Canada Foundation for Innovation grant (CFI 37115) to T. R. P. T. R. P. acknowledges Canada Research Chair Program.

CONFLICT OF INTEREST STATEMENT

The authors declare no conflict of interest.

DATA AVAILABILITY STATEMENT

The data that support the findings of this study are available from the corresponding author upon reasonable request. SAXS data and models have been provided to SASDB server and can be accessed using the following links.

https://www.sasbdb.org/data/SASDQJ6/nnpq5x7r7b
https://www.sasbdb.org/data/SASDQK6/3c3g5bau73
https://www.sasbdb.org/data/SASDQL6/rl94ryjlap
https://www.sasbdb.org/data/SASDQM6/42lksc9z1t

ORCID

Higor Sette Pereira https://orcid.org/0000-0003-4761-8361
Darren L. Gemmill https://orcid.org/0000-0003-2834-9063
M. Quadir Siddiqui https://orcid.org/0000-0003-0891-3122
Gunjan Vasudeva https://orcid.org/0000-0002-1404-0498
Trushar R. Patel http://orcid.org/0000-0003-0627-2923

REFERENCES

1. Sklenovská N, Van Ranst M. Emergence of monkeypox as the most important orthopoxvirus infection in humans. *Front Public Health*. 2018;6:241.
2. Breman JG, Kalisa-ruti R, Steniowski MV, Zanotto E, Gromyko AI, Arita I. Human monkeypox, 1970-79. *Bull World Health Organ*. 1980;58(2):165-182.

3. Bunge EM, Hoet B, Chen L, et al. The changing epidemiology of human monkeypox—a potential threat? A systematic review. *PLoS Neglected Trop Dis*. 2022;16(2):e0010141.
4. Reed KD, Melski JW, Graham MB, et al. The detection of monkeypox in humans in the Western Hemisphere. *N Engl J Med*. 2004;350(4):342-350.
5. Kozlov M. Monkeypox goes global: why scientists are on alert. *Nature*. 2022;606(7912):15-16.
6. Alakunle EF, Okeke MI. Monkeypox virus: a neglected zoonotic pathogen spreads globally. *Nat Rev Microbiol*. 2022;20(9):507-508.
7. Alakunle E, Moens U, Nchinda G, Okeke MI. Monkeypox virus in Nigeria: infection biology, epidemiology, and evolution. *Viruses*. 2020;12(11):1257.
8. Rimoin AW, Mulembakani PM, Johnston SC, et al. Major increase in human monkeypox incidence 30 years after smallpox vaccination campaigns cease in the Democratic Republic of Congo. *Proc Natl Acad Sci*. 2010;107(37):16262-16267.
9. Dai Y, Teng X, Hu D, Zhang Q, Li J. A peculiar evolutionary feature of monkeypox virus. *bioRxiv*. 2022.
10. Spiegel J, Adhikari S, Balasubramanian S. The structure and function of DNA G-Quadruplexes. *Trends Chem*. 2020;2(2):123-136.
11. Balaratnam S, Basu S. Divalent cation-aided identification of physico-chemical properties of metal ions that stabilize RNA G-quadruplexes. *Biopolymers*. 2015;103(7):376-386.
12. Bhattacharyya D, Mirihana Arachchilage G, Basu S. Metal cations in G-Quadruplex folding and stability. *Front Chem*. 2016;4:38.
13. Lombardi EP, Londoño-Vallejo A. A guide to computational methods for G-quadruplex prediction. *Nucleic Acids Res*. 2020;48(3):1603.
14. Meier-Stephenson V, Badmalia MD, Mrozowich T, et al. Identification and characterization of a G-quadruplex structure in the pre-core promoter region of hepatitis B virus covalently closed circular DNA. *J Biol Chem*. 2021;296:100589.
15. Holoubek J, Bednářová K, Haviernik J, et al. Guanine quadruplexes in the RNA genome of the tick-borne encephalitis virus: their role as a new antiviral target and in virus biology. *Nucleic Acids Res*. 2022;50(8):4574-4600.
16. Rhodes D, Lipps HJ. G-quadruplexes and their regulatory roles in biology. *Nucleic Acids Res*. 2015;43(18):8627-8637.
17. Nakanishi C, Seimiya H. G-quadruplex in cancer biology and drug discovery. *Biochem Biophys Res Commun*. 2020;531(1):45-50.
18. Saranathan N, Vivekanandan P. G-Quadruplexes: more than just a kink in microbial genomes. *Trends Microbiol*. 2019;27(2):148-163.
19. Wang SR, Zhang QY, Wang JQ, et al. Chemical targeting of a G-Quadruplex RNA in the Ebola virus L gene. *Cell Chem Biol*. 2016;23(9):1113-1122.
20. Artusi S, Ruggiero E, Nadai M, et al. Antiviral activity of the G-Quadruplex ligand TMPyP4 against Herpes Simplex virus-1. *Viruses*. 2021;13(2):196.
21. Majee P, Pattnaik A, Sahoo BR, et al. Inhibition of Zika virus replication by G-quadruplex-binding ligands. *Molecular Therapy-Nucleic Acids*. 2021;23:691-701.
22. Lv L, Zhang L. G-quadruplexes in the monkeypox virus are potential antiviral targets. *J Med Virol*. 2023;95(1):e28299.
23. Shammas MA, Shmookler Reis RJ, Akiyama M, et al. Telomerase inhibition and cell growth arrest by G-quadruplex interactive agent in multiple myeloma. *Mol Cancer Ther*. 2003;2(9):825-833.
24. Kikin O, D'Antonio L, Bagga PS. QGRS mapper: a web-based server for predicting G-quadruplexes in nucleotide sequences. *Nucleic Acids Res*. 2006;34(Web Server issue):W676-W682.
25. Garant JM, Perreault JP, Scott MS. Motif independent identification of potential RNA G-quadruplexes by G4RNA screener. *Bioinformatics*. 2017;33(22):3532-3537.
26. Katoh K, Standley DM. MAFFT multiple sequence alignment software version 7: improvements in performance and usability. *Mol Biol Evol*. 2013;30(4):772-780.
27. Nguyen LT, Schmidt HA, von Haeseler A, Minh BQ. IQ-TREE: a fast and effective stochastic algorithm for estimating maximum-likelihood phylogenies. *Mol Biol Evol*. 2015;32(1):268-274.
28. Letunic I, Bork P. Interactive tree of life (iTOL) v5: an online tool for phylogenetic tree display and annotation. *Nucleic Acids Res*. 2021;49(W1):W293-W296.
29. Xiao S, Zhang J, Zheng K, Hao Y, Tan Z. Bioinformatic analysis reveals an evolutional selection for DNA:RNA hybrid G-quadruplex structures as putative transcription regulatory elements in warm-blooded animals. *Nucleic Acids Res*. 2013;41(22):10379-10390.
30. Altschul SF, Gish W, Miller W, Myers EW, Lipman DJ. Basic local alignment search tool. *J Mol Biol*. 1990;215(3):403-410.
31. Sievers F, Wilm A, Dineen D, et al. Fast, scalable generation of high-quality protein multiple sequence alignments using Clustal Omega. *Mol Syst Biol*. 2011;7:539.
32. Meier M, Moya-Torres A, Krahn NJ, et al. Structure and hydrodynamics of a DNA G-quadruplex with a cytosine bulge. *Nucleic Acids Res*. 2018;46(10):5319-5331.
33. Franke D, Petoukhov MV, Konarev PV, et al. ATSAS 2.8: a comprehensive data analysis suite for small-angle scattering from macromolecular solutions. *J Appl Crystal*. 2017;50(Pt 4):1212-1225.
34. Panjkovich A, Svergun DI. CHROMIXS: automatic and interactive analysis of chromatography-coupled small-angle X-ray scattering data. *Bioinformatics*. 2018;34(11):1944-1946.
35. Putnam CD. Guinier peak analysis for visual and automated inspection of small-angle X-ray scattering data. *J Appl Crystal*. 2016;49(pt 5):1412-1419.
36. Burke JE, Butcher SE. Nucleic acid structure characterization by small angle X-ray scattering (SAXS). *Curr Protoc Nucleic Acid Chem*. 2012;51(1):7-18.
37. Svergun DI. Determination of the regularization parameter in indirect-transform methods using perceptual criteria. *J Appl Crystal*. 1992;25(4):495-503.
38. Franke D, Svergun DI. DAMMIF, a program for rapid ab-initio shape determination in small-angle scattering. *J Appl Crystal*. 2009;42(pt 2):342-346.
39. Volkov VV, Svergun DI. Uniqueness of ab initio shape determination in small-angle scattering. *J Appl Crystal*. 2003;36(3-1):860-864.
40. Del villar-Guerra R, Trent JO, Chaires JB. G-Quadruplex secondary structure obtained from circular dichroism spectroscopy. *Angew Chem Int Ed*. 2018;57(24):7171-7175.
41. Kim DN, Thiel BC, Mrozowich T, et al. Zinc-finger protein CNBP alters the 3-D structure of lncRNA Braveheart in solution. *Nat Commun*. 2020;11(1):148.
42. D'Souza MH, Mrozowich T, Badmalia MD, et al. Biophysical characterisation of human LincRNA-p21 sense and antisense Alu inverted repeats. *Nucleic Acids Res*. 2022;50(10):5881-5898.
43. Mohanty J, Barooah N, Dhamodharan V, Harikrishna S, Pradeepkumar PI, Bhasikuttan AC. Thioflavin T as an efficient inducer and selective fluorescent sensor for the human telomeric G-quadruplex DNA. *J Am Chem Soc*. 2013;135(1):367-376.
44. Lattmann S, Giri B, Vaughn JP, Akman SA, Nagamine Y. Role of the amino terminal RHAU-specific motif in the recognition and resolution of guanine quadruplex-RNA by the DEAH-box RNA helicase RHAU. *Nucleic Acids Res*. 2010;38(18):6219-6233.
45. Giri B, Smaldino PJ, Thys RG, et al. G4 resolvase 1 tightly binds and unwinds unimolecular G4-DNA. *Nucleic Acids Res*. 2011;39(16):7161-7178.
46. Mori K, Gotoh S, Yamashita T, et al. The porphyrin TMPyP4 inhibits elongation during the noncanonical translation of the FTLD/ALS-associated GGGGCC repeat in the C9orf72 gene. *J Biol Chem*. 2021;297(4):101120.
47. Mackett M, Archard LC. Conservation and variation in Orthopoxvirus genome structure. *J Gen Virol*. 1979;45(3):683-701.

48. Shchelkunov SN, Totmenin AV, Safronov PF, et al. Analysis of the monkeypox virus genome. *Virology*. 2002;297(2):172-194.
49. Suraweera CD, Anasir MI, Chugh S, et al. Structural insight into tanapoxvirus-mediated inhibition of apoptosis. *FEBS J*. 2020; 287(17):3733-3750.
50. Beaudoin JD, Jodoin R, Perreault JP. New scoring system to identify RNA G-quadruplex folding. *Nucleic Acids Res*. 2014;42(2):1209-1223.
51. Bedrat A, Lacroix L, Mergny JL. Re-evaluation of G-quadruplex propensity with G4Hunter. *Nucleic Acids Res*. 2016;44(4):1746-1759.
52. Lago S, Nadai M, Ruggiero E, et al. The MDM2 inducible promoter folds into four-tetrad antiparallel G-quadruplexes targetable to fight malignant liposarcoma. *Nucleic Acids Res*. 2021;49(2):847-863.
53. Ahsendorf H, Gan L, Eltom K, et al. Species-specific conservation of linear antigenic sites on vaccinia virus A27 protein homologs of orthopoxviruses. *Viruses*. 2019;11(6):493.
54. Kastenmayer RJ, Maruri-Avidal L, Americo JL, Earl PL, Weisberg AS, Moss B. Elimination of A-type inclusion formation enhances cowpox virus replication in mice: implications for orthopoxvirus evolution. *Virology*. 2014;452-453:59-66.
55. Moss B. Poxvirus DNA replication. *Cold Spring Harbor Perspect Biol*. 2013;5(9):a010199.
56. Abrahim M, Guterres A, da Costa Neves PC, Ano Bom APD. The emergence of new lineages of the Monkeypox virus could affect the 2022 outbreak. *bioRxiv*. 2022.
57. Xu S, Li Q, Xiang J, et al. Thioflavin T as an efficient fluorescence sensor for selective recognition of RNA G-quadruplexes. *Sci Rep*. 2016;6:24793.
58. Chen MC, Tippana R, Demeshkina NA, et al. Structural basis of G-quadruplex unfolding by the DEAH/RHA helicase DHX36. *Nature*. 2018;558(7710):465-469.
59. Mou X, Kwok CK. Effect of RNA sequence context and stereo-chemistry on G-quadruplex-RHAU53 interaction. *Biochem Biophys Res Commun*. 2020;533(4):1135-1141.
60. Morris MJ, Wingate KL, Silwal J, Leeper TC, Basu S. The porphyrin TmPyP4 unfolds the extremely stable G-quadruplex in MT3-MMP mRNA and alleviates its repressive effect to enhance translation in eukaryotic cells. *Nucleic Acids Res*. 2012; 40(9):4137-4145.

SUPPORTING INFORMATION

Additional supporting information can be found online in the Supporting Information section at the end of this article.

How to cite this article: Pereira HS, Gemmill DL, Siddiqui MQ, Vasudeva G, Patel TR. Mapping and characterization of G-quadruplexes in monkeypox genomes. *J Med Virol*. 2023;95:e28783. doi:10.1002/jmv.28783